SAND2017-11570J

Strain-rate sensitivity of strength dependence on the softening factor c_b in Ti-alloy wires

A.F. Jankowski[1], J.M. Chames[1], and E.M. Brannigan[2]
[1]Sandia National Laboratory, P.O. Box 969 MS-9161, Livermore, CA 94551-0969
[2]Los Alamos National Laboratory, P.O. Box 1663, Los Alamos, NM 87545

Abstract

Titanium alloys such as Ti-6Al-4V and Ti-6Al-7Nb are widely used in the biomedical industry as structural implant materials. The strain-rate sensitivity of tensile strength is now assessed using a modified Kocks-Mecking formulation for hardening. The operative scale of the microstructural strengthening is designated by the coefficieint $\mathbf{c_b}$ that can be determined from measurements of plastic strain, yield and ultimate strength. It is found that although that strength varies slightly with strain rate, the scale of the microstructure $\mathbf{c_b}$ remains nearly constant for each material. A low $\mathbf{c_b}$-value of 14 is computed for Ti-6Al-4V that is consistent with the refined two-phase microstructure needed to enhance both ductility beyond yielding and its ultimate strength.

Keywords*: softening factor; strain-rate sensitivity; plasticity; Ti alloys*

Introduction

Titanium (Ti) alloys are widely used in the aerospace, marine, chemical, biological and sporting goods industries [Poondla, et al. (2009)]. Ti and its alloys are used for bone and tooth replacement since the quasi static mechanical properties are similar to those of bone and Ti alloys have excellent osseo integration, i.e. the ability to bond with bone over time [Le Guehennec, et al. (2007)] is favorable due to the crystalline structure and oxide layer that provide the ability to self-repair by re oxidation when damaged [Leventhal (1951); Breme (1998); Browne and Gregson (2000)]. In addition, Ti causes fewer allergic reactions than other implant materials [Evrard, et al. (2010); Gawkrodger (2005)] in the form of swelling or toxicity on macrophages and fibroblasts in patients. Some two-phase (α-β) Ti alloys are better suited for implantation since the properties of pure Ti don't exactly match the mechanical properties of bone. The stabilization of two-phase Ti alloys is accomplished by solute additions such as aluminum (Al) an α-stabilizer, and vanadium (V) a β-stabilizer. The most common Ti-based alloy, grade 5 Ti-6Al-4V, consists of 6 wt.% Al, 4 wt.% V, and 90 wt.% Ti. Even though grade 5 Ti-6Al-4V has excellent compatibility with human bone, the low wear resistance coupled with motion of implants relative to the implant site means [Guo, et al. (2001)] that these implants do not have lifetimes near the length-scale of an average human life. For example, the most common failure mode for total hip arthroplasty (THA) implants [Grupp, et al. (2010)] is surface micro motions such as scratching, or high loading. While oxide and nitride coatings can increase both surface hardness and improve corrosion resistance, Ti implants remain at risk for tensile failure or being rejected by the body during the period of time after implantation (i.e. during osseo integration) when the bone grows around the implant. The use of niobium (Nb) as a solute addition is reported [Matsuno, et al. (2001); Eisenbarth, et al. (2004)] to make a more biocompatible alloy than Ti-6Al-4V. The alloy Ti-6Al-7Nb alloy consists of 6 wt.% Al and 7

wt.% Nb and is found [Semlitsch, et al. (1975)] to decrease allergic reactions such as swelling and implant rejection due to decreased toxicity and increased biocompatibility.

The mechanical properties of metals are traditionally measured using near-static conditions. The ASTM E8-01 standard strain rate is 0.5 $mm \cdot mm^{-1} \cdot min^{-1}$, i.e. $8.3 \cdot 10^{-3}$ s^{-1}, for the tensile testing [ASTM (2001)] of metallic materials. Quasi-static tensile test results [Salem, et al. (2003)] indicate that Ti-6Al-7Nb has an elastic modulus of 105 GPa, grade 4 commercially pure Ti has a modulus of 104 GPa, and Ti-6Al-4V has a modulus of 114 GPa. However, the strain-rate sensitivity of strength for Ti and its alloys have received [Chichili, et al. (1998)] relatively little attention. Real-world loading conditions for implants and bone inside the human body can vary widely from the ASTM standard strain rate for metals. Impact loading such as running or jumping can produce [Wright and Hayes (1976)] a strain rate of 10^2 s^{-1} or more. The assessment of strain-rate dependent strength for these biocompatible Ti alloys is of practical interest for better reliability and longer life of orthopedic and dental implants [Strietzel, et al. (1998)].

The assessment of Ti alloy strength-structure behavior as a function of strain rate is now pursued further to enable advancements in biomedical applications such as hard implant coatings. The strengthening model used in the assessment of strain rate is based on the Kocks-Mecking model as modified [Morris, Jr. (2007)] to identify the operative scale of microstructure in two-phase metal alloys, as originally developed for refining second-phase particulates below the micron scale to assess the practicality of producing high-strength and ductile "nanosteels. The use of tensile testing is pursued across four-orders of magnitude in strain rate – where the yield strength, plastic strain and ultimate strength are used to determine a softening factor $\mathbf{c_b}$, i.e. a characteristic scale of the nano-, micro- structure. The strain rate sensitivity dependence of $\mathbf{c_b}$ will be evaluated for the first time in the strain-rate dependent tensile testing of Ti and alloy wires.

Strengthening and structure model

The focus of the application is to determine the operative scale of the microstructure that is responsible for the measured changes in strengthening with variable strain rate as based on the modified [Morris, Jr. (2007)] Kocks-Mecking model for the work-hardening function as applied to the case of two-phase microstructures. The representative value is the softening coefficient $\mathbf{c_b}$ as computed using the yield strength $\boldsymbol{\sigma_y}$, and the true plastic strain $\boldsymbol{\varepsilon_u}$ as measured from the yield point to the ultimate tensile strength $\boldsymbol{\sigma_u}$ of the wires according to the expression

$$\boldsymbol{\varepsilon_u} = (\mathbf{c_b})^{-1} \cdot \{\ln[1 + \mathbf{c_b} \cdot (1 - \boldsymbol{\sigma}^*)\} \qquad (1)$$

The reduced stress $\boldsymbol{\sigma}^*$ equals the ratio of the yield to ultimate strength, i.e. $(\boldsymbol{\sigma_y}/\boldsymbol{\sigma_u})$. The expression is derived [Morris, Jr. (2007)] using the Considère criteria. That is, the stress-strain construct that uses the tangent method to determine yield point. Analysis of eqn. (1) shows that $\boldsymbol{\varepsilon_u}$ is maximized as $\boldsymbol{\sigma}^*$ goes to zero. This infers that use of the second phase is optimized to increase the ultimate strength of the alloy well beyond the initial yield point as effectively determined by the matrix phase. For the case of "nanosteels", this could be represented [Morris, Jr. (2007)] by a fine distribution of a martensitic-phase particles that are incoherent with the

parent ferritic matrix. Similarly, for the present case, a maximum amount of plastic strain can be obtained for a fine distribution of second-phase Ti alloy particles in a ductile matrix phase. The contributing structural parameter of eqn. (1) is the softening coefficient $\mathbf{c_b}$ where its effect on maximizing plastic strain is found for decreasing values. In general, it's anticipated that nanostructured alloys will have $\mathbf{c_b}$ values less than 10. The determination of $\mathbf{c_b}$ across a wide strain-rate range of testing will provide information as to whether or not the underlying structure changes its effect on strengthening as, e.g., through processes as dynamic recrystallization.

Characterization of structure

The microstructural features and composition of the as-received nominally (0.994 pure) Ti, (grade 5) Ti-6Al-4V, and Ti-6Al-7Nb alloy welding wires are examined using a scanning electron microscope (SEM). 250 mm segments of the 1.0-1.2 mm diameter wire are used in tensile experiments. The pure Ti and Ti-6Al-4V wires are reportedly hot drawn, whereas the Ti-6Al-7Nb wire was cold drawn. The specific structure and composition of each alloy wire is relevant only within the context to the interpretation of the softening factor ($\mathbf{c_b}$) value, i.e. in what manner $\mathbf{c_b}$ changes with the strain-rate analysis of strength for the tensile tests. A detailed determination of the process-structure history is not needed here. The low-angle (below-the-lens) secondary-electron detector, imaging mode (LEI) enhances surface relief from the polished samples that were treated using a low-contrast, Kroll's etchant. A dilute acid solution of 6% nitric and 2% hydrofluoric was swabbed onto each sample surface for 10-15 s. Before etching the polished surfaces, x-ray diffraction (XRD) scans are conducted in the $\boldsymbol{\theta}/2\boldsymbol{\theta}$ mode using Cu $K\alpha$ radiation over a 30°-90° range of $2\boldsymbol{\theta}$. The XRD scans reveal the crystalline Bragg reflections of the constituent alloys, the presence of texturing in the wire, and the presence of multiple alloy phases. The analyses are conducted in directions along (axial) and transverse (radial) to the wire axis.

X-ray diffraction analysis

The Ti wire is a polycrystalline hexagonal close-packed (hcp) structure, i.e. the α-phase. Basal plane (00.2) texturing along the axial direction is evident in the XRD scan of Fig. 1. The additional reflections observed in Fig. 1 for the pure Ti wire match those reported [Sandim, et al (2005); Jafari, et al (2010)] for the α-phase, where the peak positions (as labeled and indicated with dashed lines) for pure Ti are computed using lattice parameters **a** = 0.2952 nm and **c** = 0.4681 nm. The radial direction shows (10.0) texturing, complimentary to the (00.2) texturing found for the radial section.

The addition of alloying elements as Al, V, and Nb to the α-phase of Ti can produce alloys with multiple phases. The lattice parameters of the α-phase in the alloy can change [Gallegos, et al (2012); Rangaswamy, et al. (1999); Shan, et al. (2007); Yang, et al (2016); Zhu and Li (2009)] to values of **a** = 0.292-0.293 nm and **c** = 0.466-0.472 nm. The possible increase in **c** and slight decrease in **a** for the α-phase Ti alloy wires will tend to shift the (00.2) peak to a lower $2\boldsymbol{\theta}$ position, and increase the $2\boldsymbol{\theta}$ position of the (20.1) peak, both of which are seen in Fig. 1 when comparing the Ti alloy to the pure Ti wire scans. In addition, the presence of the fcc Ti(Al) phase is reported [Chen, et al. (2004); Jankowski and Wall (1994, 1996); Zhang and Ying (2002); Yu,

et al. (2017)] for nanocrystalline structures as well as (severely plastically-deformed) ball-milled Al-Ti powders. The presence of Al and/or a face-centered-cubic (fcc) Ti(Al) alloy phase is possible (in Fig. 1) as indicated by the γ-phase labeling of peak positions for the (111) and (200) reflections as computed [Chen, et al. (2004); Yu, et al. (2017)] using a lattice parameter **a** = 0.409 nm. Alternatively, a 0.440 nm lattice parameter will produce a (111) reflection at a 2**θ** position of 44.2°.

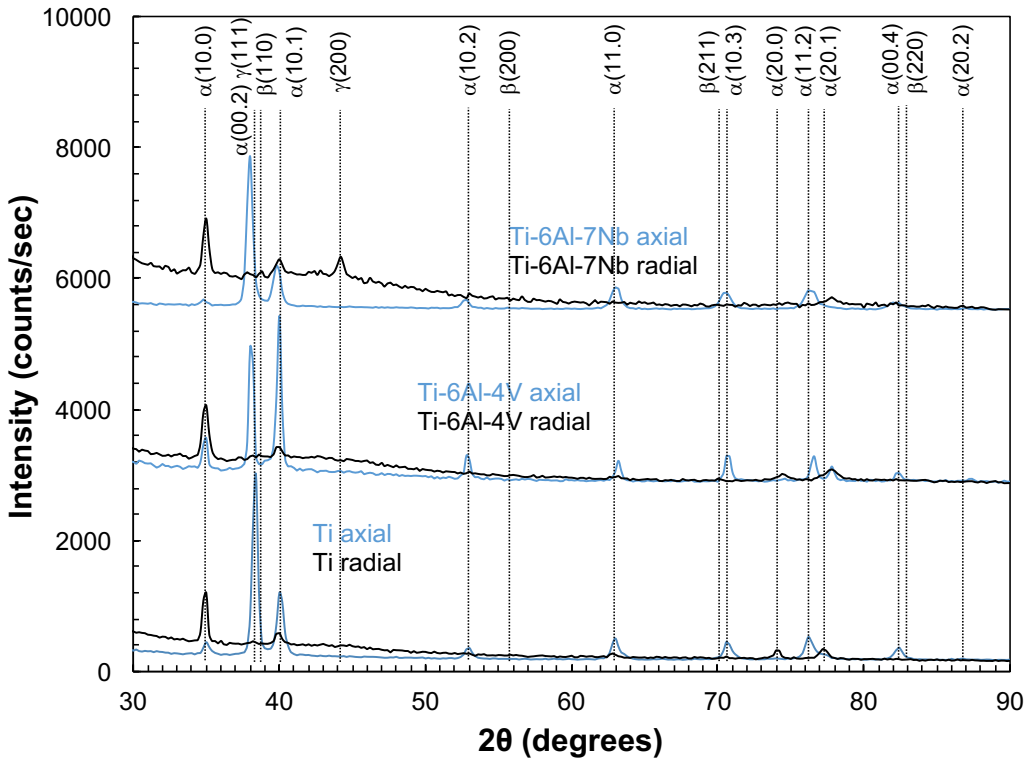

Figure 1. X-ray diffraction scans **θ**/2**θ** mode of the Ti, Ti-6Al-4V, and Ti-6Al-7Nb alloy wires as examined in the axial (blue curve) and radial (black curve) sections, respectively.

The presence of a body-centered-cubic (bcc) β-phase for the Ti-6Al-4V [Zhu and Li (2009)] and Ti-6Al-7Nb [Gallegos, et al (2012)] alloy wires would appear in the XRD scans where peak positions are computed using the lattice parameter **a** = 0.329 nm. Possible evidence of the β-phase in the alloy wires may be found for the diffuse 2**θ** peak of the (110) reflection that is found between the (00.2) and (10.1) α-phase reflections. The addition of bcc stabilizing elements as V and Nb lowers the α-to-β phase transformation temperature producing α-β-phase alloy wires. The strong peak intensities of the characteristic α-phase in the Ti alloy wires would suggest a minor β-phase component to a possible bimodal α-β phase distribution.

Electron micrographs

The SEM micrographs of Fig. 2 are obtained in the LEI imaging mode at a 8mm working distance using a 5 keV incident electron beam. The LEI mode enhances definition of the grain structure and appearance of secondary phase(s). Each sample is viewed in both the axial (as

oriented left-to-right in the top row) and radial sections (in the bottom row). The pure Ti wire has an elongated grain structure as seen in the axial view of Fig. 2a, and the appearance of a refined grain structure in the Fig. 2d radial section view. Secondary phases may appear as particles [Gammon, et al. (2004); Shan, et al. (2007)] that can be attributed to impurity-stabilized β-phase and/or a Ti-hydride phase.

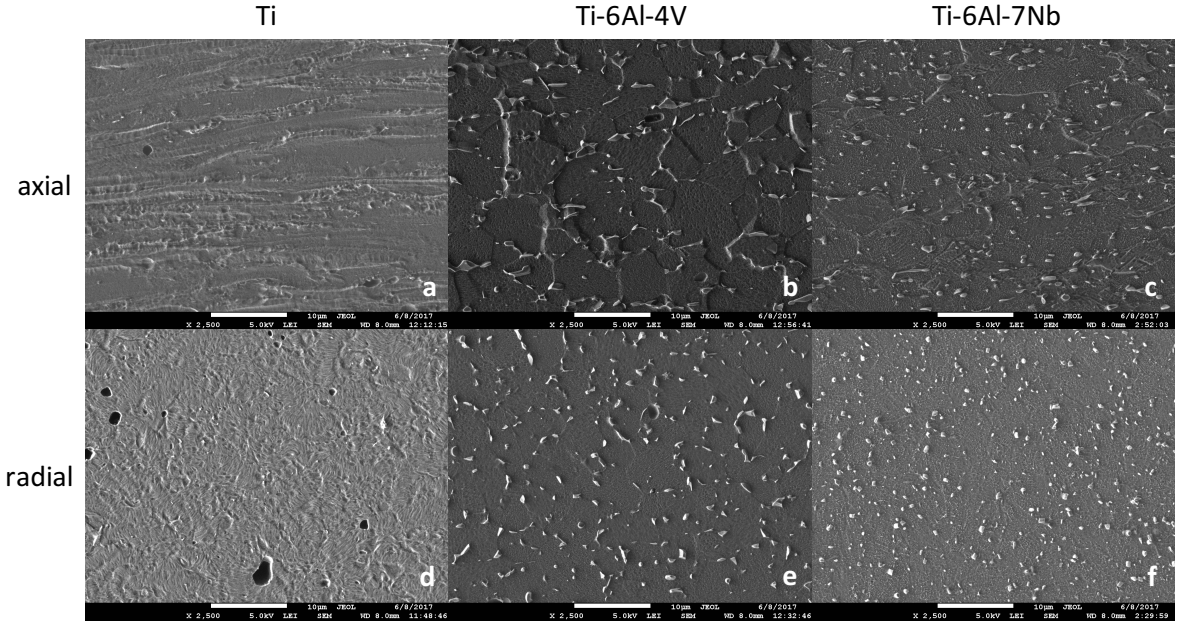

Figure 2. Scanning electron micrographs of the Ti, Ti-6Al-4V, and Ti-6Al-7Nb alloy wires as imaged in the LEI mode along the (a-c) axial and (d-f) radial sections, respectively. Bar = 10 μm.

The presence of a distinct Widmanstätten α-phase structure in the Ti alloy wire samples is not clearly resolvable in the Fig. 2 images. An equiaxed, i.e. a globular or primary, α-phase structure is routinely found [Chávez-Díaz, et al. (2017); Collins, et al. (2009)] as seen in Figs. 2b,e for Ti-6Al-4V and Figs. c,f for Ti-6Al-7Nb. A mean linear intercept calculation is often used common to determine the average size of the constituent structure. The typical formulation includes a shape factor since the grains are assumed to be a geometric variant of spheres-to-cubes. An estimate is made for the matrix phase of each Ti wire material without the shape factor since the true shape geometry is unknown. The axial section images of Figs. 2a-c provide mean linear intercept values of 1.1±0.1 μm for the width to the banded structure of pure Ti, 3.1±0.3 μm for near equiaxed structure of Ti-6Al-4V, and 1.9±0.2 μm for the width to the slightly elongated structure of Ti-6Al-7Nb.

A bimodal structure is seen in the Figs. 2b,e images that is representative of a dual phase Ti-6Al-4V alloy. Similar microstructures are found in specimens that have been forged [Gammon, et al. (2004); Shan, et al. (2007)] or in this case, cold-drawn. Surface relief is seen with a second particulate phase at, or near, the grain boundaries. The Fig. 2 structures such as that seen in Fig. 2e can be encountered for α-particles in a β-matrix; or particles in a martensitic α′-matrix where in the later case would require a rapid quench from temperatures above the β-to-α phase transus. In addition, β-precipitates are seen [Pederson (2002)] at grain boundaries in a primary (90%) α-

phase matrix for Ti-6Al-4V heated to 550 °C, held at temperature, and then slow cooled. Similar images, but with a more-refined grain structure, are seen in the Fig. 2c,2f images of the Ti-6Al-7Nb alloy wire. However, in the radial views, there is the distinct appearance of a second, perhaps a β-fleck, alloy phase that appears throughout the predominately matrix structure.

Composition analysis

Composition analysis will tie together the results of the XRD and SEM images that appear to indicate a minor presence of a particulate β-phase in a α-phase matrix. Energy dispersive spectrometry (EDS) is used to probe the elemental composition of the Ti, Ti-6Al-4V, and Ti-6Al-7Nb wires. The characteristic x-ray peaks up to a 10 keV energy were collected as emitted from the matrix, and particle phases that appear in the Figs. 2e-f images. The x-ray peaks of interest that are used in this analysis are the 1.49 keV Al $K\alpha_1$, 2.17 keV Nb $L\alpha_1$, V $K\alpha_1$, and 4.51 keV Ti $K\alpha_1$. The weight percent values computed using the intensities of these characteristic x-rays are listed in Table 1. A ±0.5 wt.% error is the measured value for precision in this EDS analysis.

Table 1. Weight % composition of the Ti-alloy wires from characteristic x-rays

X-ray line	Ti-6Al-4V		Ti-6Al-7Nb	
	matrix	particle	matrix	particle
Ti $K\alpha_1$	92.9	82.5	86.4	74.1
Al $K\alpha$	3.4	2.6	6.2	4.7
V	3.7	14.1	-	-
Nb $L\alpha_1$	-	-	7.4	18.2
Fe $K\alpha$	-	0.8	-	3.0

X-ray maps of the Ti-6Al-4V and Ti-6Al-7Nb surfaces indicate a (diffuse) enhancement of V and Nb, respectively, in the second phase particulates that appear in Figs. 2e-f. In addition to the Al, Nb, V and Ti x-rays, the presence of characteristic 0.62 keV $L_{111}l$, 0.71 keV L_{111ab}, 0.72 keV L_{11ab}, 6.40 keV $K\alpha$, and 7.06 keV $K\beta_1$ peaks for Fe are found in the particle spectra of the Ti-6Al-4V and Ti-6Al-7Nb wires. The lower Al content and much higher-base content of the β-stabilizing elements V (14 wt.% versus 7 wt.%) and Nb (18 wt.% versus 7 wt.%) in the smaller particulates versus matrix phases may be evidence for β-segregation [Gammon, et al. (2004)]. The wt.% composition values are found to be consistent with microprobe measurements [Elmer, et al (2005)] of the α- and β-phases in a (grade 5) Ti-6Al-4V alloy where the matrix is found to be 6.7wt.%Al-1.4wt.%V and the particle is 2.9wt.%Al-15.4wt.%V-1.3wt.%Fe.

Mechanical testing

Tensile testing is used to measure the plastic strain, yield stress, and ultimate strength. The wire samples are mounted according to ASTM standards using a wire spool grip, a gage length of 92-122 mm, and loading at varying rates from 10^{-5} to 10^{-1} s^{-1}. The diameters of the Ti, Ti-6A-4V, and Ti-6Al-7Nb wires are measured where the nominal values are 1.19 mm, 0.88 mm, and 1.02 mm, respectively. To achieve this strain-rate range, a nominal 24 mm displacement of the wire is

applied over time intervals that range from 5-to-4000 sec. These rates are consistent with limits for the minimum and maximum velocities of the tensile test instrument. The results of a single wire tensile test contain three regions that include: an initial nonlinear pre-loading region where the wrapped ends of the wire are brought under tension removing slack in the wire; a linear elastic loading section; and a deformation section after yielding where the wire strain hardens and plastically deforms until failure. The logarithmic variation of change in yield strength $\boldsymbol{\sigma_y}$ with increasing strain rate $\dot{\varepsilon}$ is used to determine the strain-rate sensitivity coefficient **m** using the Dorn equation. Although $\boldsymbol{\sigma_y}$ can vary due to grain size variation (i.e. the Hall-Petch effect) and surface finish, the stock wire material is assumed to be invariant in these attributes. The values of engineering stress $\boldsymbol{\sigma_e}$ and strain $\boldsymbol{\varepsilon_e}$ are determines using the measured load **P**, the initial wire diameter **d**, the gage length **l**, and the displacement of the wire Δ**l** during loading. A linear regression analysis is used to isolate the elastic loading regime. Once the non-linear behavior begins, i.e. the wire begins to yield at the proportional limit, the measure of plastic strain to failure is recorded. In addition, the offset method is used to determine the yield point as well. A typical tensile load **P** versus displacement **z** curve is shown in Figure 3. The **P**-**z** curve is shown as plotted beyond the initial pre-loading region for a 1.19 mm dia. pure Ti wire as tested at a strain rate $\dot{\varepsilon}$ of $1.19 \cdot 10^{-2}$ s^{-1}. The dashed red curves are used to determine the proportional limit and origin (i.e. zero elastic displacement), the proportional limit, and the ultimate strength, as well as the deformation range of plastic strain.

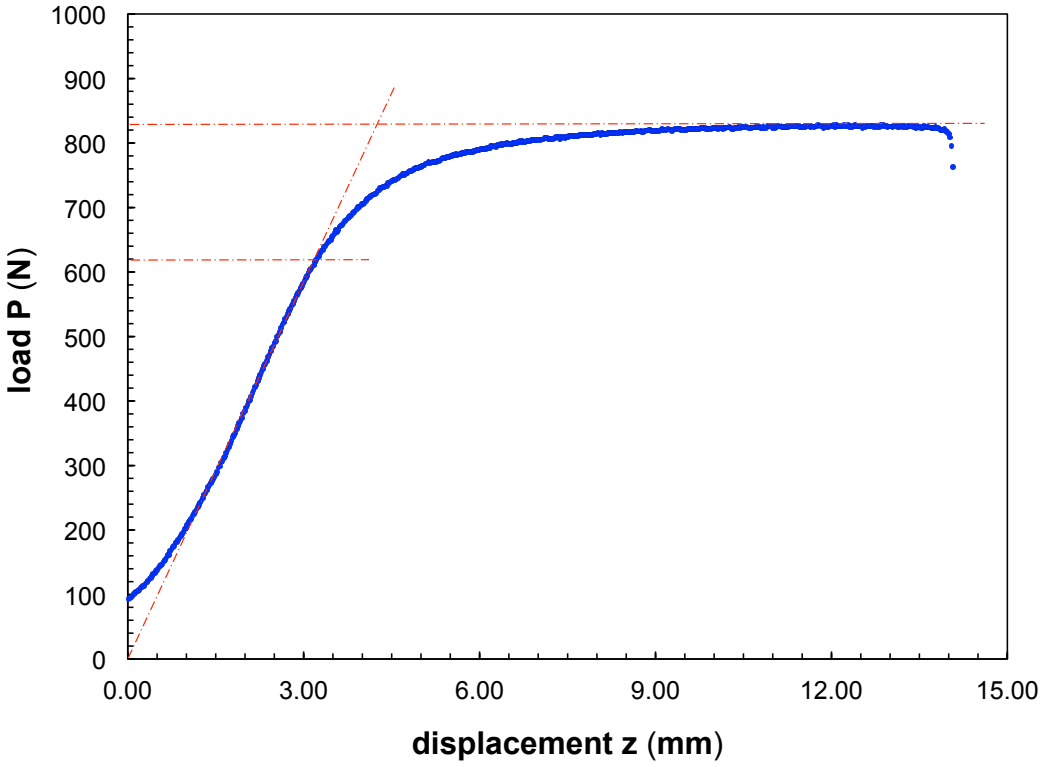

Figure 3. A load **P**-displacement **z** curve for the tensile testing of a pure Ti wire using a strain rate of $1.19 \cdot 10^{-2}$ s^{-1}.

Several tensile tests of the pure Ti and alloy wires are displayed in stress-strain plots of Figure 4 as tested across a range of strain rates (that are indicated in the figure). The top three curves are

for Ti-6Al-7Nb, the middle three curves are for Ti-6Al-4V, and the bottom three curves are for pure Ti. The yield point is determined using the proportional limit since there can be considerable work-hardening effects to the hcp based-matrix in each wire during the tensile test.

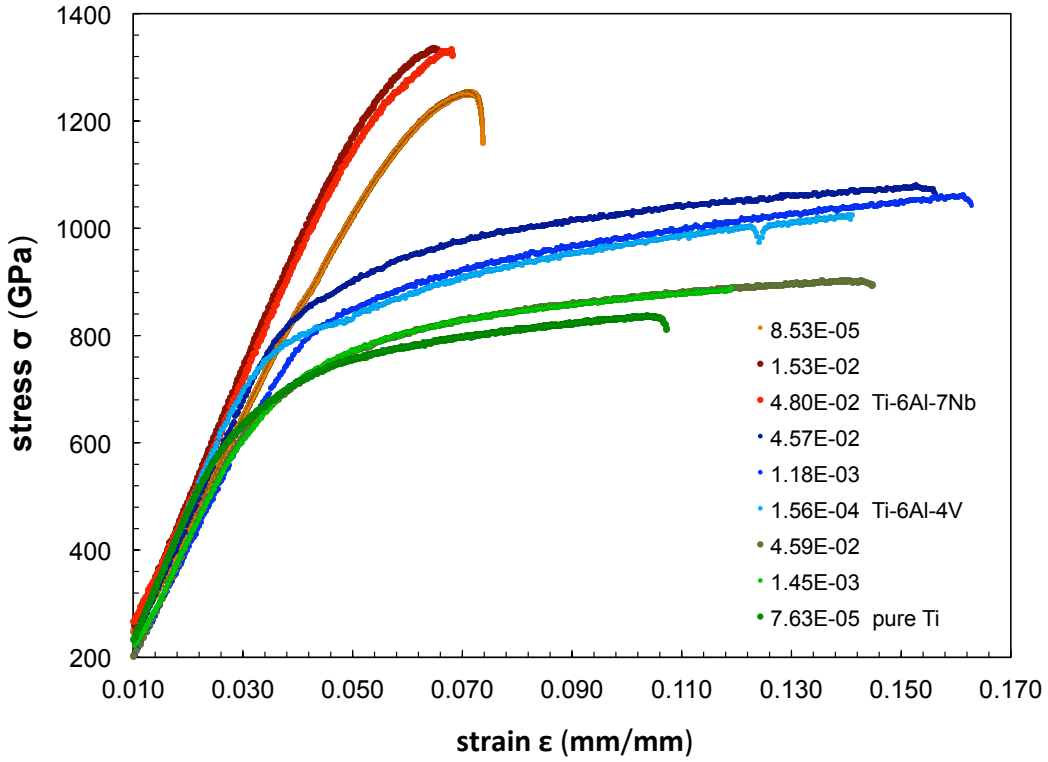

Figure 4. Stress-strain curves for the tensile testing of Ti-6Al-7Nb, Ti-6Al-4V, and pure Ti wires where the strain rate are indicated in the figure legend.

The proportional limits for the tensile tests, across the range of strain rates used, show that commercially pure Ti exhibits the lowest yield strengths of 570-680 MPa, the Ti-6Al-4V yield strength have values of 710-830 MPa, and the Ti-6Al-7Nb wires have yield strengths of 850-1070 MPa. The amount of plastic strain is reduced from greater than 0.10 for the Ti and Ti-6Al-4V wires to less than 0.04 for the Ti-6Al-7Nb wires.

In general, it is seen in Figure 4 that the yield strength $\boldsymbol{\sigma_y}$ increases with strain rate $\dot{\varepsilon}$. This strain-rate effect on strengthening is quantified using the ln-ln scale relationship of the Dorn equation, i.e. $\boldsymbol{\sigma_y} = \dot{\varepsilon}^{\mathbf{m}}$, as plotted in Figure 5. The slope of each linear curve in Figure 5 is the exponent $\mathbf{m}$ of the strain-rate sensitivity relationship, $\mathbf{m} = (\ln \boldsymbol{\sigma_y})/(\ln \dot{\varepsilon})$. The Ti-6Al-7Nb has the least strain-rate sensitivity with an exponent $\mathbf{m}_{\mathrm{Ti6Al7Nb}}$ of -0.008 ± 0.007 whereas pure Ti and the Ti-6Al-4V wires behave similarly with exponents of $\mathbf{m}_{\mathrm{Ti}} = 0.014 \pm 0.006$, and $\mathbf{m}_{\mathrm{Ti6Al4V}} = 0.014 \pm 0.008$, respectively.

From the yield strength and strain rate data, the activation volume $\boldsymbol{\upsilon}^*$ for the onset of plastic deformation can be computed [Cahn and Nabarro (2001)] using the relationship

$$\boldsymbol{\upsilon}^* = (\mathbf{k_B}\cdot\mathbf{T})\cdot[\partial(\ln \dot{\varepsilon})/\partial(\boldsymbol{\sigma})] \qquad (2)$$

At room temperature, the product of Boltzmann's constant $\mathbf{k_B}$ and temperature **T**, i.e. $\mathbf{k_B \cdot T}$, equals $4.142 \cdot 10^{-21}$ J or 4.142 MPa·nm^3. The corresponding activation volume **υ*** is therefore the product of $\mathbf{k_B \cdot T}$ with the slope of linear curves plotted in Figure 6 for the ln strain rate versus yield strength data.

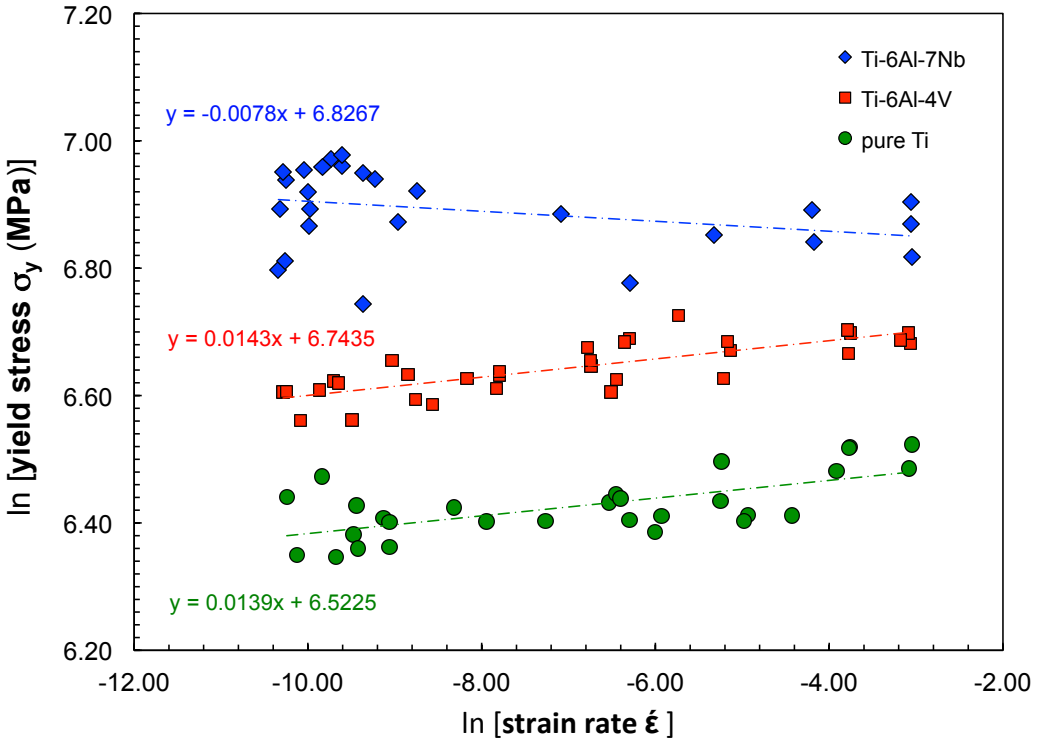

Figure 5. The strain-rate sensitivity of strength exponent **m** is the slope of the linear-curve fit to the ln-ln variation of tensile yield stress with strain rate for the Ti-6Al-7Nb (blue top curve), Ti-6Al-4V (red middle curve), and pure Ti (green bottom curve) wires.

The values of **υ*** computed from Figure 6 for the pure Ti, and Ti-6Al-4V wires are 0.207 ± 0.117 nm^3, and 0.230 ± 0.090 nm^3, respectively. Assuming a typical magnitude of the Burger's vector $|\mathbf{b}|$ that is equal to approximately 0.2 nm, these **υ*** values correspond to activation volumes of 26-29 $\mathbf{b}^3$ dislocations. A **υ*** value for the Ti-6Al-7Nb wires was not calculated since the strain-rate sensitivity exponent $\mathbf{m_{Ti6Al7Nb}}$ from Figure 5 was approximately zero producing an indeterminate slope for the Figure 6 data.

The Kocks-Mecking relationship is now used to provide the scale of the underlying microstructure through the softening coefficient $\mathbf{c_b}$ that is responsible for the hardening of the wire during tensile testing. The $\mathbf{c_b}$ value is fitted in Equation (1) to produce the measured plastic strain the using the values measured for the yield and ultimate strength from tensile test curves as shown in Figure 4. The variation of $\mathbf{c_b}$ across the range of strain rates used during tensile testing is plotted in Figure 7. It is seen that the values remain approximately constant across the full range of strain rates used in these wire tensile tests. The $\mathbf{c_b}$ values for pure Ti, Ti-6Al-4V, and the Ti-6Al-7Nb wires are 19, 14, and 135, respectively.

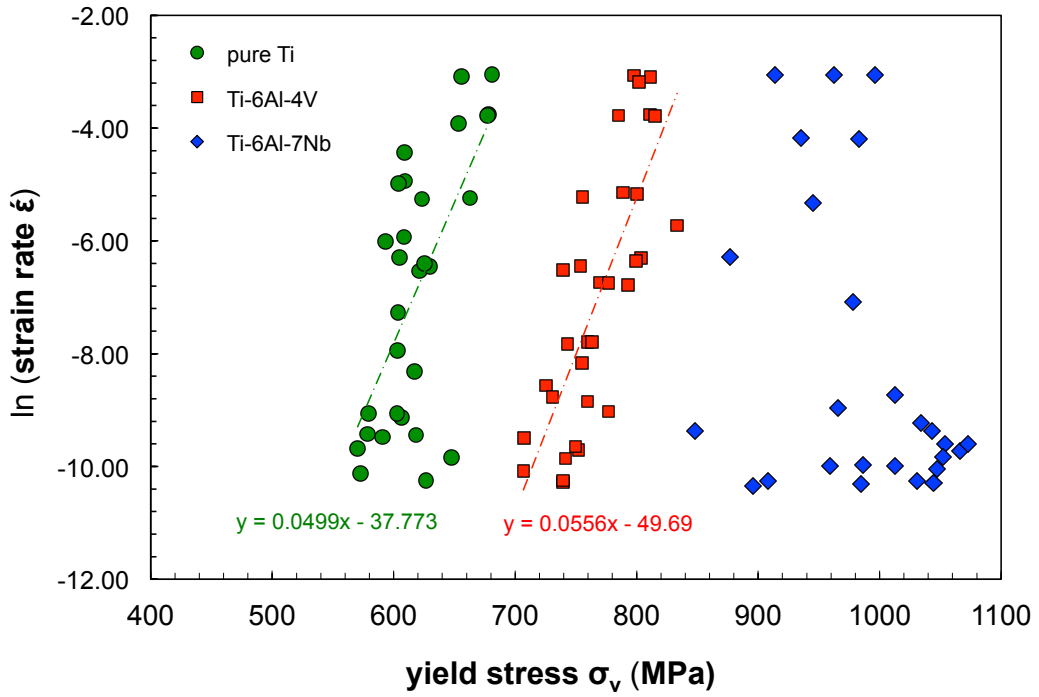

Figure 6. The activation volume υ^* that corresponds with strain-rate sensitivity of strength is computed as a product of $\mathbf{k_B \cdot T}$ with the slope of the linear-curve fit to the ln strain rate variation with strength for Ti-6Al-4V (red curve), and pure Ti (green curve).

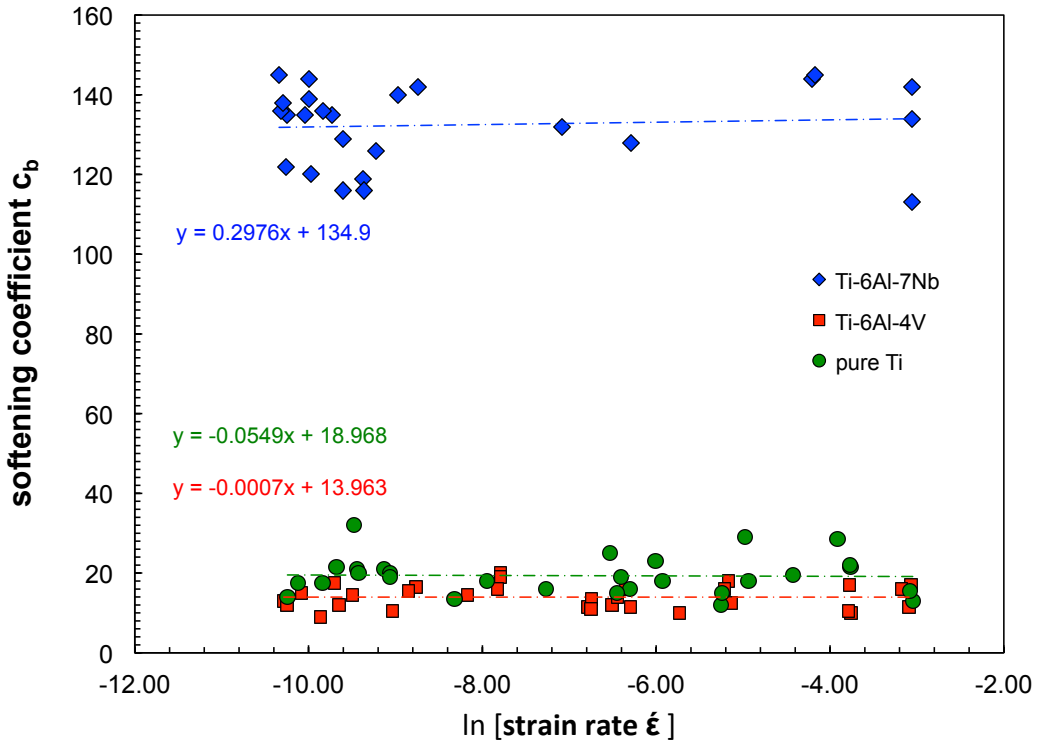

Figure 7. The softening coefficient $\mathbf{c_b}$ is plotted as function of the strain rate during tensile testing of the Ti-6Al-7Nb (green data), Ti-6Al-4V (red data), and pure Ti (blue data) wires.

Discussion

The microstructure of the wires used in this study is consistent with an α-phase matrix, and a dispersion of β-phase particulates decorating the grain boundaries. The orthonormal diffraction scans show texturing consistent with material that has been wire drawn. A refined microstructure for all of the wires is seen with a characteristic grain size on the order of a few microns, with a submicron size for the secondary β-phase. The enrichment of V and Nb is found in the β-phase particles using EDS measurements similar to microprobe measurements [Elmer, et al. (2005)] of Ti-6Al-4V alloys.

The variation in strength between the tensile test samples, as for the sample lot of Ti-6Al-7Nb wire, is consistent [Collins, et al. (2009)] with a microstructure of an equiaxed α-phase (that is ~70% by volume fraction) which can cause a concurrent variation in tensile strength between 910-980 MPa. The limited ductility of the Ti-6Al-7Nb wire is consistent with its cold-drawn processing versus greater plasticity found for the hot-drawn pure Ti and Ti-6Al-4V wires. The greater ductility and variance between yield and ultimate strength for the Ti-6Al-4V wires should correspond [Morris Jr, (2007)] to a smaller softening coefficient $\mathbf{c_b}$ as modeled using the modified Kocks-Mecking expression of Equation (1). The measured values for the Ti-alloy wires are consistent with this behavior where $\mathbf{c_b}$-values of 14 and 135 are computed for Ti-6Al-4V and Ti-6Al-7Nb, respectively. Although the SEM images of the microstructure show similar scales of structure consistent with the enhanced strength of the Ti-6Al-7Nb alloy versus the Ti-6Al-4V wire, only the $\mathbf{c_b}$-values reveal the clear difference that is seen in the plasticity and reduce stress ratio $\boldsymbol{\sigma}^*$ between the yield and ultimate strengths.

The strain rate sensitivity coefficients **m** for the Ti-alloy system are low at less than 0.015 for all samples. These low **m** values and the near constant $\mathbf{c_b}$-values for each Ti-alloy would indicate the strength is nearly invariant from slow through fast strain rates, i.e. 10^{-5}-10^{-1} s^{-1}, that are associated with standard-to-impact loading conditions for biomedical applications. The low $\mathbf{c_b}$-value of 14 for the Ti-6Al-4V wires and corresponding small activation volume of ~$29\mathbf{b}^3$ is consistent with the micron-scale matrix and submicron-scale particle phase as proposed [Morris, Jr. (2007)] to optimize the ultimate strength and plasticity of nano steel alloys, or in general, two-phase nanostructured materials.

Summary

The predictable behavior of Ti-alloy wires into the impact loading regime is key for successful application in the biomedical industry as structural implant materials. The tensile testing of Ti-alloy wires is pursued to evaluate the variance in microstructure that contributes to changes in strength as a function of strain rate from 10^{-5}-10^{-1} s^{-1}. The structure of the wires is characterized using x-ray diffraction and scanning electron microscopy imaging and composition analysis. The strain-rate sensitivity of tensile strength is assessed using the Dorn relationship to determine the strain rate sensitivity coefficient **m**, the Cahn-Nabarro formulation of activation volume $\boldsymbol{\upsilon}^*$ for the onset of plasticity, and through a Morris, Jr. modified formulation of the Kocks-Mecking

relationship where the operative scale of the microstructure for plasticity from yield to ultimate strength is designated by the softening coefficient $\mathbf{c_b}$. The plasticity of the hot-drawn pure Ti and Ti-6Al-4V wires exceeds 10%, whereas the cold drawn Ti-6Al-7Nb wires is less than 4%. The Ti-6Al-4V yield strength ranges from 710-830 MPa, and the Ti-6Al-7Nb wires have yield strengths of 850-1070 MPa. A high $\mathbf{c_b}$-value of 135 is computed for the softening coefficient of Ti-6Al-7Nb as indicated by its limited plasticity. It is found that although that wire strength increases slightly with strain rate as seen in a low **m**-value of 0.015, the scale of the microstructure $\mathbf{c_b}$ remains nearly constant for each alloy. A low $\mathbf{c_b}$-value of 14 is found for Ti-6Al-4V that is consistent with a small υ^*-value of 29 $\mathbf{b}^3$ the refined two-phase microstructure needed to enhance both ductility and ultimate strength.

Acknowledgments

The authors thank A. Gardea, and A. Kilgo of Sandia National Laboratories for their assistance in preparing the metallographic samples of the Ti-alloy wires. The microscopy and data analysis for this work was performed at Sandia National Laboratory in Livermore, CA. Sandia National Laboratories is a multi-mission laboratory managed and operated by National Technology and Engineering Solutions of Sandia, LLC., a wholly owned subsidiary of Honeywell International, Inc., for the U.S. Department of Energy's National Nuclear Security Administration under contract DE-NA0003525.

References

ASTM E8-01, "Standard Test Methods for Tension Testing of Metallic Materials", ASTM International, West Conshohocken, PA (2001) DOI: 10.1520/E0008-01

J. Breme, E. Steinhauser, G. Paulus, "Commercially pure titanium Steinhauser plate-screw system for maxillofacial surgery", Biomaterials (1998) 9:310-313

M. Browne, P.J. Gregson, "Effect of mechanical surface pretreatment on metal ion release", Biomaterials (2000) 21:385-392

J.W. Cahn, F. Nabarro, "Thermal activation under shear", Philosophical Magazine (2001) A81:1409-1426

M.P. Chávez-Díaz, M.L. Escudero-Rincón, E.M. Arce-Estrada, R. Cabrera-Sierra, "Osteoblast cell response on the Ti-6Al-4V alloy heat-treated", Materials (2017) 10:445-1-10

Z.P. Chen, Z. wen, Q. Jiang, "Phase stabilities of fcc Ti nanocrystals", Solid State Communications (2004) 132:747-750

D.R. Chichili, K.T. Ramesh, K.J. Hemker, "The high-strain-rate response of alpha-titanium: experiments, deformation mechanisms and modeling", Acta Materialia (1998) 46:1025-1043

P.C. Collins, B. Welk, T. Searless, J. Tiley, J.C. Russ, H.L. Fraser, "Development of methods for the quantification of microstructural features in α+β-processed α/β titanium alloys", Materials Science and Engineering A (2009) 50:174-182

E. Eisenbarth, D. Velten, M. Müller, R. Thull, J. Breme, "Biocompatibility of β-stabilizing elements of titanium alloys", Biomaterials (2004) 25:5705-5713

J.W. Elmer, T.A. Palmer, S.S. Babu, E.D. Specht, "In situ observations of lattice expansion and transformation rates of α and β phases in Ti-6Al-4V", Materials Science and Engineering A (2005) 391:104-113

L. Evrard, D.E. Waroquier, D. Parent, "Allergies to dental metals. Titanium: a new allergen", Rev. Med. Brux. (2010) 31:44-49

V.M.C.A. de Oliveira, M.C.L. da Silva, C.G. Pinto, P.A. Suzuki, J.P.B. Machado, V.M. Chad, M.J.R. Barboza, "Short-term creep properties of Ti-6Al-4V alloy subjected to surface plasma carburizing process", Journal of Materials Research and Technology (2015) 4:359-366

J. Gallego, T.S. Pinheiro, R.Z. Valiev, V. Polykova, C. Bolfarini, C.S. Kiminami, A.M. Jorge Jr., W.J. Botta, "Microstructural characterization of Ti-6Al-7Nb alloy after severe plastic deformation", Materials Research (2012) 15:786-791

L.M. Gammon, R.D. Briggs, J.M. Packard, K.W. Batson, R. Boyer, C.W. Domby, "Metallography and microstructures of titanium and its alloys", ASM Handbook, Metallography and Microstructure, ed. G.F. Vander Voort, ASM International, Metals Park, OH (2004) 9:899-917

D.J. Gawkrodger, "Investigation of reactions to dental materials", Br. J. Dermatol. (2005) 153:479-485

T.M. Grupp, T. Weik, W. Bloemer, H.P. Knaebel, "Modular titanium alloy neck adapter failures in hip replacement-failure mode analysis and influence of implant material", BMC Musculoskelet Disord. 4 (2010) 11:3-1-12

L. Le Guehennec, A. Soueidan, P. Layrolle, Y. Amouriq, "Surface treatments of titanium dental implants for rapid osseointegration", Dental Materials (2007) 27:844-854

C. Guo, J. Zhou, J. Zhao, L. Wang, Y. Yu, J. Chen, "Improvement of the oxidation and wear resistance of pure Ti by laser-cladding Ti_3Al coating at elevated temperature", J. Tribol. Lett. (2011) 42:151–159

M. Jafari, M. Vaezzadeh, S. Noroozizadeh, "Thermal stability of α phase of titanium by using x-ray diffraction", Metallurgical and materials Transactions A (2010) 41:3287-3290

A.F. Jankowski, M.A. Wall, "Formation of face-centered-cubic titanium on a Ni single crystal and in Ni/Ti multilayers", Journal of Materials Research (1994) 9:31-38

A.F. Jankowski, M.A. Wall, “Synthesis and characterization of nanophase face-centered-cubic titanium”, Nanostructured Materials (1996) 7:89-94

G.S. Leventhal, “Titanium, a metal for surgery”, J. Bone Joint Surg. Am. (1951) 33:473-474

H. Matsuno, A. Yokoyama, F. Watari, M. Uo, T. Kawasaki, “Biocompatibility and osteogenesis of refractory metal implants, titanium, hafnium, niobium, tantalum and rhenium”, Biomaterials (2001) 22: 1253-1262

J.W. Morris, Jr., “Is there a future for nanostructured steel?”, 16th International Society for Offshore and Polar Engineering (ISOPE) Conference Proceedings (2007) 2814-2818

R. Pederson, “Microstructure and phase transformation of Ti-6Al-4V”, Licentiate thesis, Luleå Univ. Technol. (2002) p.21

N. Poondla, T.S. Srivatsan, A. Patnaik, M. Petraroli, “A study of the microstructure and hardness of two titanium alloys: Commercially pure and Ti–6Al–4V”, Journal of Alloys and Compounds (2009) 486: 162-167

P. Rangaswamy, M.B. Prime, M. Daymond, M.A.M. Bourke, B. Clausen, H. Choo, N. Jayaraman, “Comparison of residual strains measured by x-ray and neutron diffraction in a titanium (Ti-6Al-4V) matrix composite”, Materials Science and Engineering A (1999) 259:209-219

A.A. Salem, S.R Kalidindi, R.D. Doherty, “Strain hardening of titanium: Role of deformation twinning”, Acta Materialia (2003) 51:4225-4237

H.R.Z. Sandim, B.V. Morante, P.A. Suzuki, “Kinetics of thermal decomposition of titanium hydride powder using in situ high-temperature x-ray diffraction (HTXRD)”, Materials Research (2005) 8:293-297

M. Semlitsch, F. Staub, H. Weber, “Titanium–aluminium–niobium alloy development for biocompatible, high strength surgical implants”, Biomedizinische Technik / Biomedical Engineering (1985) 30:334–339

D.B. Shan, Y.Y. Zong, T.F. Lu, Y. Lv, “Microstructural evolution and formation mechanism of fcc titanium hydride in Ti-6Al-4V-xH alloys”, Journal of Alloys and Compounds (2007) 427:229-234

R. Strietzel, A. Hosch, H. Kalbfleisch, D. Buch, “In vitro corrosion of titanium”, Biomaterials (1998) 19:1495-1499

T.M. Wright, W.C. Hayes, “Tensile testing of bone over a wide range of strain rates: effects of strain rate, microstructure and density”, Medical and Biological Engineering and Computing (1976) 14:671–680

H.C. Wu, A. Kumar, J. Wang, X.F. Bi, C.N. Tomé, Z. Zhang, S.X. Mao, “Rolling-induced face centered cubic titanium in hexagonal close packed titanium at room temperature”, Scientific Reports (2016) 6:24370-1-8

J. Yang, H. Yu, J. Yin, M. Gao, Z. Wang, X. Zeng, “Formation and control of martensite in Ti-6Al-4V alloy produced by selective laser melting”, Materials and Design (2016) 108:308-318

Q. Yu, J. Kacher, C. Gammer, R. Traylor, A. Samanta, Z. Yang, A.M. Minor, “In situ TEM observation of fcc Ti formation at elevated temperatures”, Scripta Materialia (2017) 140:9-12

D.L. Zhang, D.Y. Ying, “Formation of fcc titanium during heating high energy ball milled Al-Ti powders”, Materials Letters (2002) 52:329-333

T. Zhu and M. Li, “Effect of 0.770 wt.% H addition on the microstructure of Ti-6Al-4V alloy and mechanism of δ-hydride formation,” Journal of Alloys and Compounds (2009) 481:480-485